

1

2

**Solid Earth**

3

**Supplementary Materials for**

4

5 **Recovery of high-resolution magnetic anomalies over an oceanic**  
6 **ridge region using an equivalent source technique and crust age**  
7 **model constraint**

8

9 **Duan Li<sup>1</sup>, Jinsong Du<sup>1,2</sup>, Chao Chen<sup>1</sup>, Qing Liang<sup>1</sup>, and Shida Sun<sup>3</sup>**

10

11 <sup>1</sup> Hubei Subsurface Multi-scale Imaging Key Laboratory, Institute of Geophysics and  
12 Geomatics, China University of Geosciences, Wuhan 430074, China

13 <sup>2</sup> State Key Laboratory of Geological Processes and Mineral Resources, China  
14 University of Geosciences, Wuhan 430074, China

15 <sup>3</sup> Hebei Key Laboratory of Strategic Critical Mineral Resources, Hebei GEO  
16 University, Shijiazhuang 050031, China

17

18 **Correspondence:** Jinsong Du (jinsongdu@cug.edu.cn)

19 **1 Calculation of the magnetic anomaly caused by a cuboid**

20 In this study, the forward calculation method of the magnetic anomaly field produced  
 21 by a homogeneous prism (Bhattacharyya, 1964; Rao and Babu, 1991) was used to  
 22 construct the synthetic field and equivalent sources (ESs). Based on the assumption  
 23 that the prism is uniformly magnetized, its magnetization direction is defined by the  
 24 inclination  $I$  and declination  $D$ . The components of the magnetic field in the Cartesian  
 25 coordinate system can be expressed by the following equations:

$$26 \quad B_x(x, y, z) = \frac{\mu_0 m}{4\pi} \left[ \arctan \frac{(\xi - x)(\eta - y)}{(\xi - x)^2 + r(\zeta - z) + (\zeta - z)^2} \cos I \cos D \right. \\ \left. + \ln[r + (\zeta - z)] \sin I \cos D + \ln[r + (\eta - y)] \sin I \right] \sin I \left| \frac{\xi_2}{\xi_1} \right| \frac{\eta_2}{\eta_1} \left| \frac{\zeta_2}{\zeta_1} \right|, \quad (S1)$$

$$27 \quad B_y(x, y, z) = \frac{\mu_0 m}{4\pi} \left[ \ln[r + (\zeta - z)] \cos I \cos D \right. \\ \left. + \arctan \frac{(\xi - x)(\eta - y)}{(\eta - y)^2 + r(\zeta - z) + (\zeta - z)^2} \sin I \cos D, \right. \\ \left. + \ln[r + (\xi - x)] \sin I \right] \sin I \left| \frac{\xi_2}{\xi_1} \right| \frac{\eta_2}{\eta_1} \left| \frac{\zeta_2}{\zeta_1} \right|, \quad (S2)$$

$$28 \quad B_z(x, y, z) = \frac{\mu_0 m}{4\pi} \left[ \ln[r + (\eta - y)] \cos I \cos D + \ln[r + (\xi - x)] \sin I \cos D \right. \\ \left. - \arctan \frac{(\xi - x)(\eta - y)}{r(\zeta - z)} \sin I \right] \sin I \left| \frac{\xi_2}{\xi_1} \right| \frac{\eta_2}{\eta_1} \left| \frac{\zeta_2}{\zeta_1} \right|, \quad (S3)$$

29 where  $r$  is the Euclidean distance between the integrated  $(\xi, \eta, \zeta)$  and observation  $(x, y,$   
 30  $z)$  points,  $\mu_0$  is the permeability in vacuum, and  $m$  is the magnetization of the prism.

31 The total-field magnetic anomaly  $\Delta B$  is approximated based on the projection of the  
 32 anomalous magnetic vector in the direction of the main geomagnetic field ( $B_0$ ). The  
 33 forward analytic equation is as follows:

$$34 \quad \Delta B(x, y, z) = B_y \sin I_0 \sin D_0 + B_x \cos I_0 \cos D_0 + B_z \sin I_0, \quad (S4)$$

35 where the parameters  $I_0$  and  $D_0$  are the inclination and declination of the main

36 geomagnetic field ( $B_0$ ), respectively.

37

## 38 **2. Inversion strategy**

39 To solve large equations, a damping term is often used to stabilize the inversion  
40 process (e.g., von Frese et al., 1988; Mendonca and Silva, 1994; Oliveira Jr et al.,  
41 2013; Siqueira et al., 2017; Tikhonov and Arsenin, 1977). Therefore, the objective  
42 function can be written as:

$$43 \phi(\mathbf{m}) = \|(\mathbf{d} - \mathbf{G}\mathbf{m})\|_2^2 + \lambda \|\mathbf{m}\|_2^2, \quad (\text{S5})$$

44 where the first term on the right is the squared Euclidean norm of the difference  
45 between the observed data  $\mathbf{d}$  and predicted data  $\mathbf{G}\mathbf{m}$  and  $\lambda$  is the damping or  
46 regularization factor.

47 Equation S5 can be minimized by setting  $\nabla\phi(\mathbf{m}) = 0$ :

$$48 \nabla\phi = \nabla[(\mathbf{d} - \mathbf{G}\mathbf{m})^T(\mathbf{d} - \mathbf{G}\mathbf{m}) + \lambda \mathbf{m}^T\mathbf{m}] = \mathbf{G}^T\mathbf{G}\mathbf{m} - \mathbf{G}^T\mathbf{d} + \lambda\mathbf{m} = 0$$

49 Consequently,  $\mathbf{m}$  can be determined by solving the following equation:

$$50 (\mathbf{G}^T\mathbf{G} + \lambda\mathbf{I})\mathbf{m} = \mathbf{G}^T\mathbf{d} \quad (\text{S6})$$

51 By adding  $\lambda$ , the increase in the condition number ( $\mathbf{G}^T\mathbf{G} + \lambda\mathbf{I}$ ) can be reduced and the  
52 inversion process can be stabilized.

53 A precondition matrix is adopted in the inversion process to balance the decay of  
54 the forward kernel matrix  $\mathbf{G}$  (Silva et al., 2014) and improve the inversion efficiency.  
55 By multiplying the preconditioned matrix  $\mathbf{P}$  on both sides of Eq. (S6), Eq. (7) is  
56 obtained:

$$57 \mathbf{P}(\mathbf{G}^T\mathbf{G} + \lambda\mathbf{I})\mathbf{m} = \mathbf{P}\mathbf{G}^T\mathbf{d}, \quad (\text{S7})$$

58 where  $\mathbf{P}$  is the diagonal matrix. The diagonal element of  $\mathbf{P}$  is  $z^\beta$ , where  $z$  is the central  
 59 depth of the ES cell and  $\beta$  is the weighting index, which can be determined based on  
 60 the attenuation characteristics of the potential field generated by the corresponding ES  
 61 cell (e.g., [Liu et al., 2015](#); [Li et al., 2020](#)).

62 Given the specificity of the study area, a constraint should be introduced into the  
 63 ES model to enhance the “strip” features by using flatness weights. A simplified  
 64 constraint is used, which is based on the model objective function proposed by Li and  
 65 Oldenburg (1996):

$$66 \quad \phi_m = \int_v w_x \left| \frac{\partial m}{\partial x} \right|^2 dv + \int_v w_y \left| \frac{\partial m}{\partial y} \right|^2 dv. \quad (\text{S8})$$

67 By dividing the ES layer into discrete cells,  $\phi_m$  can be represented by diagonal  
 68 and difference matrices. The objective function can be rewritten as follows:

$$69 \quad \phi(\mathbf{m}) = \|(\mathbf{d} - \mathbf{G}\mathbf{m})\|_2^2 + \lambda(\|\mathbf{W}_x\mathbf{m}\|_2^2 + \|\mathbf{W}_y\mathbf{m}\|_2^2), \quad (\text{S9})$$

70 where  $w_x$  and  $w_y$  are the factors controlling the flatness values between adjacent cells  
 71 in the ES model in two horizontal directions, respectively.

72 By minimizing  $\phi(\mathbf{m})$  and adding the precondition matrix, Eq. (S10) is obtained:

$$73 \quad \mathbf{P}[\mathbf{G}^T\mathbf{G} + \lambda(\mathbf{W}_x^T\mathbf{W}_x + \mathbf{W}_y^T\mathbf{W}_y)]\mathbf{m} = \mathbf{P}\mathbf{G}^T\mathbf{d}, \quad (\text{S10})$$

74 where each component matrix ( $\mathbf{W}_x$  and  $\mathbf{W}_y$ ) can be written as the product of two  
 75 individual matrices ([Li and Oldenburg, 1996](#)), that is,

$$76 \quad \mathbf{W}_i = \mathbf{S}_i\mathbf{D}_i \quad i = x, y, \quad (\text{S11})$$

77 where  $\mathbf{S}_i$  are the diagonal matrices with elements  $(w_i)^{1/2}$  and  $\mathbf{D}_i$  are the finite difference  
 78 matrixes for each direction.

79

80 **3. ES model used in the experiment**

81 In the experiment, a shallow ES layer is placed in an area with a size of  $550 \text{ km} \times 700$   
82 km. This area is larger than the area for which magnetic anomaly data is available,  
83 which is composed of 3996 cells (cuboids) with uniform horizontal sizes of 5 km (in  
84 the west–east direction) by 20 km (in the south–north direction) and a uniform  
85 thickness of 5 km. We chose a larger cell size in the south–north direction  
86 (perpendicular to the survey line) to gain a better computation efficiency in areas with  
87 sparse survey lines. The deep ES layer was further enlarged to  $1000 \text{ km} \times 1000 \text{ km}$ . It  
88 is composed of 676 cells with uniform sizes of  $40 \text{ km} \times 40 \text{ km} \times 40 \text{ km}$  and is placed  
89 at a depth of 95 km based on the power spectrum analysis of magnetic anomaly data  
90 ([Naidu, 1968](#); [Maus et al., 1997](#)).

91

92 **4. Constraint approach for the shallow ES layer**

93 The difference matrix was constructed using the backward difference. Three basic  
94 cases were used for weighting the ES cells, as shown in [Figure S1b](#). If the variation in  
95 the physical properties in blank grids (cells) reflects one of these cases, the same  
96 flatness values should be assigned to the corresponding cells. Otherwise,  $w_x = w_y = 1$   
97 is assigned to blank grids.

98

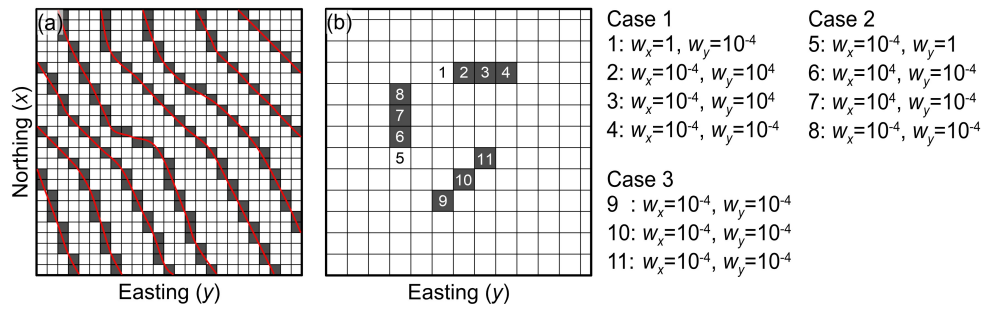


**Figure S1.** Map of the constraint approach. (a) Determination of the edge (red line) locations of magnetic lineations in the ES layer (gray grid); (b) Weighted values of the cells corresponding to three different cases.

99

## 100 References

101 Bhattacharyya, B. K: Magnetic anomalies due to prism-shaped bodies with arbitrary  
 102 polarization, *Geophysics*, 29(4), 517–531, <https://doi.org/10.1190/1.1439386>,  
 103 1964.

104 Li, D., Liang, Q., Du, J., Sun, S., Zhang, Y., and Chen, C.: Transforming Total-field  
 105 magnetic anomalies into three components using dual-layer equivalent sources,  
 106 *Geophysical Research Letters*, 47(3), e2019GL084607,  
 107 <https://doi.org/10.1029/2019GL084607>, 2020.

108 Li, Y. and Oldenburg, D. W.: 3-D inversion of magnetic data, *Geophysics*, 61(2),  
 109 394–408, <https://doi.org/10.1190/1.1443968>, 1996.

110 Liu, S., Hu, X., Xi, Y. and Liu, T.: 2D inverse modeling for potential fields on rugged  
 111 observation surface using constrained Delaunay triangulation, *Computer &  
 112 Geosciences*, 76, 18–30, <https://doi.org/10.1016/j.cageo.2014.11.010>, 2015.

113 Maus, S., Gordon, D., and Fairhead, D.: Curie-temperature depth estimation using a  
 114 self-similar magnetization model, *Geophysical Journal International*, 129(1),  
 115 163–168. <https://doi.org/10.1111/j.1365-246X.1997.tb00945.x>, 1997.

116 Mendonca, C. A. and Silva, J. B. C.: The equivalent data concept applied to the

117 interpolation of potential field data, *Geophysics*, 59(5), 722–732,  
118 <https://doi.org/10.1190/1.1443630>, 1994.

119 Oliveira Jr, V. C., Barbosa, V. C. F. and Uieda, L.: Polynomial equivalent layer,  
120 *Geophysics*, 78(1), G1–G13, <https://doi.org/10.1190/geo2012-0196.1>, 2013.

121 Naidu, P: Spectrum of the potential field due to randomly distributed sources.  
122 *Geophysics*, 33(2), 337–345, <https://doi.org/10.1190/1.1439933>, 1968.

123 Pilkington, M.: 3-D magnetic imaging using conjugate gradients, *Geophysics*, 62(4),  
124 1132–1142, <https://doi.org/10.1190/1.1444214>, 1997.

125 Rao, D. B. and Babu N. R.: A rapid method for three-dimensional modeling of  
126 magnetic anomalies, *Geophysics*, 56(11), 1729–1737,  
127 <https://doi.org/10.1190/1.1442985>, 1991.

128 Silva, J. B. C., Santos, D. F., and Garabito, G.: Harmonic and biharmonic biases in  
129 potential field inversion, *Geophysics*, 79(1), G15–G25,  
130 <https://doi.org/10.1190/GEO2013-0137.1>, 2014.

131 Siqueria, F. C. L., Oliveira Jr., V. C. and Barbosa, V. C. F.: Fast iterative  
132 equivalent-layer technique for gravity data processing: A method grounded on  
133 excess mass constraint, *Geophysics*, 82(4), G57–G69,  
134 <https://doi.org/10.1190/GEO2016-0332.1>, 2017.

135 Tikhonov, A. N. and Arsenin, V. Y.: Solution of ill-posed problem, *Mathematics of*  
136 *Computation*, 32(144), 491–491, 1977.

137 von Frese, R. R. D., Ravat, D. N., Hinze, W. J., and McGue, C. A.: Improved  
138 inversion of geopotential field anomalies for lithospheric investigations,  
139 *Geophysics*, 53(3), 375–385, <https://doi.org/10.1190/1.1442471>, 1988.